Fuel 429 (2027) 140922

Contents lists available at ScienceDirect

Fuel

journal homepage: www.elsevier.com/locate/jfue

Full Length Article

Micropore analysis of biomass chars: Physisorption measurements of N_2, CO_2, O_2, and H_2 and application of different theoretical methods

Tim Eisenbach [a,*], Ehsan Sadeghi Pouya [b], Carsten Wedler [c], Erik Freisewinkel [d], Viktor Scherer [d], Eric F. May [b], Roland Span [a]

[a] Thermodynamics, Ruhr University Bochum, Universitätsstraße 150, Bochum, 44780, Germany
[b] Fluid Science and Resources Division, Department of Chemical Engineering, The University of Western Australia, 35 Stirling Highway, Crawley, WA, 6009, Australia
[c] Institute of Technical Thermodynamics, RWTH Aachen, Schinkelstraße 8, Aachen, 52062, Germany
[d] Energy Plant Technology (LEAT), Ruhr University Bochum, Universitätsstraße 150, Bochum, 44780, Germany

HIGHLIGHTS

- Physisorption measurements with four probe gases on different microporous biomass char samples.
- Discussion of pore accessibility and sensitivity on basis of adsorption isotherms.
- Application of different analytical methods on physisorption data.
- Detailed comparison and discussion of methods for the reliable calculation of pore surface area and volume.

ARTICLE INFO

Keywords:
Biomass chars
Pore structure
Adsorption
BET theory
Dubinin-Astakhov theory
Non-local density functional theory

ABSTRACT

The pore structure of biomass particles is a key property governing their reaction behavior in thermochemical conversion processes. This study aims to assess the applicability of different physisorption measurement protocols and analytical approaches in pore structure analysis. Therefore, three samples produced in different conversion processes are investigated. The physisorption of N_2, O_2, and H_2 is measured at 77 K and CO_2 at 273 K using a commercial volumetric sorption instrument. The four probe gases exhibit distinct adsorption behavior on the investigated chars due to their physicochemical properties under the respective adsorption conditions. This study highlights the suitability of probe gases for investigating complex pore structures in biomass chars. The applied and compared analytical methods involve the BET theory, the Dubinin-Astakhov (DA) theory, and different non-local density functional theory (NLDFT)-based models. For microporous biomass chars, the applicability of the BET theory is limited by both the feasibility of reliable N_2 adsorption measurements and the inadequacy of the BET assumptions for adsorption in microporous carbons. The DA theory, based on CO_2 isotherms, provides a simple and straightforward basis for micropore analysis. The most comprehensive characterization is obtained from two-dimensional (2D)-NLDFT analysis resolving the pore size distribution (PSD) of the samples. Provided that a reliable adsorption isotherm is available, 2D-NLDFT analysis is considered the most robust method for determining pore properties compared to BET and DA. Dual-gas 2D-NLDFT analysis expands the analyzable pore width range. However, this study highlights the sensitivity of correlated models when adsorption data are affected by pore blocking or diffusion limitations.

1. Introduction

The reactivity of solid biomass fuels in conversion processes is strongly influenced by the pore structure of the char, while at the same time devolatilization and char reaction govern the evolution of pores throughout the different stages of conversion [1,2]. Biomass typically exhibits a very high volatile content, reaching up to 85 wt %, [3] which leads to the development of a pronounced microporous structure during pyrolysis [1,4,5]. In char gasification, pore structure and morphology strongly influence the diffusion of reactive gases inside the particle and the available pore surface area [6–9].

* Corresponding author.
Email address: t.eisenbach@thermo.rub.de (T. Eisenbach).

https://doi.org/10.1016/j.fuel.2026.140922
Received 12 May 2026; Received in revised form 17 July 2026; Accepted 6 August 2026
Available online 12 August 2026
0016-2361/© 2026 The Authors. Published by Elsevier Ltd. This is an open access article under the CC BY license (http://creativecommons.org/licenses/by/4.0/).

The pore structure properties, such as surface area, pore volume, and porosity, are commonly analyzed to characterize conversion processes and are correlated with parameters including burnout or devolatilization degree, temperature, and mineral content [2–4,10,11]. Despite the availability of experimental pore structure data, they are rarely integrated directly into established conversion models. Therefore, in char conversion and burnout kinetics models, pore characteristics are commonly represented by fitted parameters of the random pore model, [8,12] whereas in applications of the chemical percolation devolatilization (CPD) pyrolysis model, pore evolution emerges mechanistically from volatile release and bridge cleavage [6]. A meaningful linkage between experimental pore structure data and conversion models requires a clear understanding of the available pore structure analysis methods along with their inherent assumptions and suitability for biomass char pore structures.

In experimental pore structure analysis, different techniques are limited to a certain pore size range and should ideally be combined for a comprehensive analysis. Optical techniques like scanning or transmission electron microscopy (SEM or TEM) can provide information on the local porosity of materials and are restricted to the resolution of the images [13]. Liquid mercury intrusion at different pressures (MIP) yields the pore size distribution (PSD) of macropores, while being restricted in the pore regime of micropores and leaving behind destructed particles. The skeletal density of chars can be determined by helium pycnometry. However, it does not provide information on the pore size distribution (PSD) [14]. For micropore analysis, physisorption measurement techniques and methods are widely applied and focused in this study.

The field of gas adsorption provides a versatile set of measurement protocols applicable to materials with widely varying pore characteristics, ranging from highly ordered and homogeneous pore structures of zeolites and MOFs to heterogeneous, microporous carbons [15–17]. In the analysis of pore properties of microporous carbons derived from pyrolysis or conversion processes, the Brunauer-Emmett-Teller (BET) theory [18] applied to cryogenic N_2 physisorption measurements is widely used to determine the specific surface area of biomass chars [2, 19–21]. However, N_2 adsorption has well-documented limitations for probing microporosity, particularly due to restricted accessibility and diffusion limitations at cryogenic temperatures [22–24]. Alternatively, the characterization of micropores by CO_2 adsorption combined with the Dubinin–Astakhov (DA) or Dubinin–Radushkevich (DR) theory has long been established [1,25–27] and has been recognized as a suitable approach for micropore analysis [16]. Different probe gases like H_2 or O_2 can provide advantageous properties like enhanced diffusion or less pronounced surface interactions with functional groups. Previous studies have demonstrated that replacing N_2 with O_2 as the probe gas provides significant advantages, particularly for highly microporous biomass-derived chars [28,29]. Moreover, H_2 has already been explored as suitable for probing the smallest ultramicropores in carbon materials [28,30].

Recent progress in the development of two-dimensional (2D) nonlocal density functional theory (NLDFT) models, among others for heterogeneous carbon materials, has enabled a more detailed and reliable analysis of pore size distributions [15,31]. Such models allow the combination of different adsorption isotherms, while the optimal choice depends on the suitability of the adsorptive for probing the pore structure [31].

As already shown by Wedler and Span [32], applying different models on the adsorption isotherm data of CO_2 to biomass chars can lead to significantly different results in pore structure analysis. Generally, the analysis of carbonaceous materials incorporating complex pore structures with graphitic and amorphous domains contributing to different pore types is challenging [33]. In this study, the experimental adsorption isotherms of N_2, CO_2, O_2, and H_2 for three biomass-derived chars with different porosities were analyzed to assess their pore probing capabilities and, furthermore, their impact on the analysis of pore properties based on BET, DA, and 2D-NLDFT models. Given the variety of probe gases and theoretical models, this study systematically identifies differences, challenges, and limitations.

Table 1
The gravimetric elemental composition obtained from ultimate analysis and the weight percentages of fixed carbon (FC), volatile matter (VM), moisture (M), and ash (A) obtained from proximate analysis. w stands for weight percentage and C, H, N, S, and O stand for carbon, hydrogen, nitrogen, sulfur, and oxygen, respectively.

	Ultimate analysis					Proximate analysis			
	w_C	w_H	w_N	w_S	w_O	w_{FC}	w_{VM}	w_M	w_A
MCC-HTC-800[a]	94.8	0.8	–	–	4.4	97.4	2.0	0.6	–
TBW-1000	95.6	1.08	0.62	0.06	2.68	91.6	4.4	1.0	3.0
BW-1000	54.51	2.82	0.52	n.d.[b]	42.15	n.i.[c]	n.i.[c]	n.i.[c]	n.i.[c]

[a] mineral- and sulfur-free;
[b] not detected (n.d.);
[c] not investigated (n.i.)

2. Experimental

2.1. Materials

The first studied biomass char was a hydrochar synthesized from microcrystalline cellulose (MCC) in a hydrothermal carbonization (HTC) process and subsequent pyrolysis, carried out up to 1073 K at a heating rate of 5 K min^{-1}. The pore structure of the resulting MCC-HTC-800 char particles of 125–200 μm size is mainly formed by devolatilization of oxygen-containing groups and the graphitization of the carbon matrix during the pyrolysis process [34,35].

The second char was obtained from a gasification process of torrefied and shredded beechwood chips. The chips were torrefied (TBW) in a continuously working screw reactor under N_2 atmosphere [36] at 563 K for 30 min and subsequently gasified in a fluidized bed reactor (FBR) in a CO_2 atmosphere at 1273 K [37]. The resulting TBW-1000 char particles of 125–160 µm size develop their porosity through reactions of the solid carbon fraction with CO_2 and devolatilization of volatiles [3,37].

The third char is a product of flash pyrolysis of pulverized beechwood particles conducted in a drop tube reactor (DTR) in a CO_2 atmosphere with a heating rate of 1.5×10^{-4} K min^{-1} reaching a maximum particle temperature of approx. 1273 K. The resulting BW-1000 particles show equivalent diameters of 60–140 μm.

Proximate analyses of the samples were carried out in accordance with EN ISO 18134-3, EN ISO 18,122, and EN ISO 18,123, and ultimate analysis was performed following EN ISO 16,948. The results are shown in Table 1. It is noteworthy that proximate analysis could not be performed for BW-1000 due to the limited amount of sample produced in the DTR pyrolysis. Nevertheless, as a direct consequence of the pyrolysis process, the volatile matter (VM) is expected to be low and comparable to that of TBW-1000. In the pyrolysis of raw beechwood containing approx. 45 % cellulose and 25 % hemicellulose [3], cross-linking reactions between the earlier-decomposing, liquid-phase hemicellulose and cellulose structures occur and hinder the unrestricted release of volatiles [38]. In the subsequent cellulose decomposition, larger macromolecular fragments are formed, and oxygen-containing bounds are assumed to remain in the solid structure, contributing to the comparatively high oxygen content. The cross-linking of hemicellulose and the increasing lignin fraction during the torrefaction of beechwood lead to a higher yield of char in subsequent pyrolysis or gasification processes [36,39], which is consistent with the high proportion of fixed carbon in the TBW-1000 char (Table 1).

2.2. Volumetric adsorption measurements

The excess adsorption measurements were conducted using the volumetric gas adsorption set-up ASAP 2020, incorporating the

Table 2
The upper target pressure p_{max} in the measurement and adsorptive properties, including saturation pressure at adsorption temperature p_0, kinetic diameter d_k [40], and quadrupole moment μ [33,41].

	N_2	CO_2	H_2	O_2
p_{max} / kPa	101.2	120.0	120.0	20.5
p_0[a] / kPa	101.33	3485.1	supercrit.	20.762
d_k / Å	3.64	3.30	2.89	3.46
μ / $\times 10^{40}$ cm^2	−4.91	−13.71	2.2	−1.33

[a] calculated with REFPROP 10.0 [42] based on the reference EOS [43–46].

evaluation software by *Micromeritics*. The adsorption of N_2, O_2, and H_2 was measured at T = 77 K provided by a dewar filled with liquid N_2, whereas the CO_2 experiments were carried out at T = 273 K. Here, a thermostat unit maintained the temperature of an equivolumetric ethylene glycol–water mixture in a dewar, which was continuously monitored by a four-wire platinum resistance thermometer (Pt-100). The N_2 and O_2 isotherms were measured up to a target pressure p_{max} close to their respective saturation pressures p_0 (Table 2). In these experiments, the saturation pressures were determined using a p_0-cell connected to the measurement system (Fig. 1). The CO_2 and H_2 isotherms were measured up to a pressure of p_{max} = 120 kPa (apparatus limit). In the calculation of the relative pressure p/p_0 for CO_2, a constant value for the saturation pressure $p_{0,CO2}$ = 3485.1 kPa at T = 273 K was used. Since the adsorption of H_2 was measured above its critical temperature, the absolute pressure p_{abs} was used for analysis. Table 2 shows the gas-specific properties, including the kinetic diameter d_k and the quadrupole moment μ, considered in the analysis of the adsorption behavior (Section 4.1). ASAP 2020 is equipped with three pressure transducers with a full scale range of 133 kPa, 1.33 kPa and 0.133 kPa and a reported accuracy of 0.15 % (both larger ranges) and 0.12 % of reading. The probe gases were obtained from BOC Ltd. (Welshpool WA, Australia). N_2, H_2, and He were of ultra high purity (UHP) grade (99.999 %), O_2 was of UHP grade (99.995 %), and CO_2 was of laser grade (99.995 %). The samples were degassed under a dynamic vacuum p < 1.5 Pa for 10 h using a combination of a two-diaphragm roughing and a turbo-molecular pump, while the samples were simultaneously heated. The MCC-HTC-800 and TBW-1000 chars were exposed to an activation temperature of 523 K. To preserve the original pore structure and ensure comparability between the different adsorption measurements, BW-1000 was degassed at a lower temperature of 423 K, thereby avoiding any structural changes associated with the release of small amounts of residual tar species. Although, the primary pyrolysis was completed [3], we observed in pre-experiments small amounts of tars condensing in another volumetric sorption setup leading to failures of the sensors. The activation temperature and duration were still sufficient to completely remove physisorbed moisture as the mass of the activated BW-1000 sample could be reproduced for each measurement. Details on the measurement procedure involving the free space volume determination, the non-ideality correction of gases as well as the individual programmed gas dosing sequence and sample masses (Table S1) are given in *Supplementary Information*. The equilibration time was set to 30 s and refers to the time between consecutive pressure readings while the equilibrium is being approached. Equilibrium is attained once the pressure change per equilibration time (i.e., the first derivative) is below 0.01 % of the recorded average pressure during the interval. Both the first derivative and the average pressure are calculated using the Savitzky-Golay method referred to in *Supplementary Information*.

3. Analytical methods for physisorption data

Different adsorption theories and models for the determination of pore properties were applied to the experimental adsorption data. The software tool BET surface identification (BETSI) [47] claims an unambiguous BET surface area for microporous materials, while complying with the Rouquerol criteria [16,47]. The Dubinin-Astakhov (DA) equation derived from the Dubinin-Radushkevich (DR) theory, is a well-established method for micropore analysis of chars [16,25,27,48] and was applied to the CO_2 adsorption data. Furthermore, 2D-NLDFT methods for the determination of PSD were applied to single- and dual-gas combinations of adsorption isotherms.

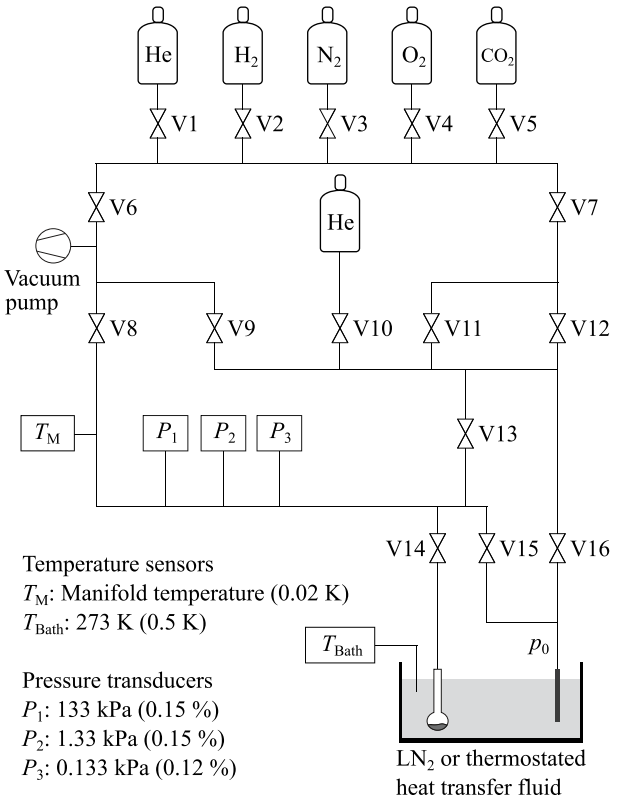


Fig. 1. Schematic of the ASAP 2020 set-up with the arrangement of all valves (V) and the temperature and pressure sensors. The temperature of the heat transfer fluid is controlled by a Pt-100 with an expanded uncertainty of 0.5 K (k = 2) and pressure transducer accuracies are given as % of the reading.

3.1. BET theory and the rouquerol criteria

The BET theory was originally developed for non-porous and meso- to macroporous solids (Type II or Type IV) [49], but can, with some limitations, be applied to microporous materials [16]. The BET equation extends the kinetic theory of monomolecular adsorption sites of the Langmuir model [50] to infinite numbers of energetically homogeneous adsorption layers establishing with increasing relative pressure p/p_0 (Eq. 1).

$$\frac{p/p_0}{n_{ads}(1-p/p_0)} = \frac{1}{n_m C} + \frac{C-1}{n_m C} p/p_0 \quad (1)$$

According to the BET theory, a monolayer of adsorbed molecules with $n_{ads} = n_m$ is established at the adsorption isotherm knee, where high values of C are associated with micropore filling of high adsorption energy at low relative pressures [16,18,51]. The characteristic region of assumed monolayer occupation of the pore surface exhibits linearity in the BET equation (Eq. 1), with multiple sections satisfying the Rouquerol criteria [52]. The BETSI software tool [47] determines the best-fitting monolayer capacity n_m in accordance with the Rouquerol criteria. The S_{BETSI} with monolayer capacity n_m, cross-sectional area of the probe molecule σ, and Avogadro constant N_a can be calculated with Eq. (2).

$$S_{BETSI} = n_m \cdot N_a \cdot \sigma \quad (2)$$

However, for microporous carbons it is rarely possible to separate the process of monolayer-multilayer adsorption and micropore filling [49]. Furthermore, as experiments can be impeded by slow diffusion and long equilibrium times, adsorption data onten do not provide reliable information of the micropore occupation. Despite its limitations, the BET theory is often applied in the analysis of pore evolution during flash pyrolysis of biomass [19–21,53]. The underlying adsorption studies exhibit low N_2 uptake [19,20], which complicates the application of the BET equation and reduces its reliability significantly. While N_2 is the most commonly used adsorptive, alternative gases such as O_2, Ar, and Kr may also be employed. This study demonstrates the ambiguity of the resulting pore structure analysis for biomass chars by applying BETSI on N_2 and O_2 adsorption isotherms.

3.2. Dubinin and Astakhov model

Based on the potential theory for the adsorbed fluid in micropores as described by Polanyi [54], Dubinin and Radushkevich [55] developed an equation for the fractional filling of the pore volume. In contrast to the BET theory, where adsorption is approached by an energetically homogeneous multilayer approach, the DR theory assumes micropores filled with an adsorbed homogeneous liquid phase. The DA equation is the generalized form of the DR theory considering stronger adsorption interaction and increased activation energy in the smallest pores by introducing an empirical constant n [56]. It is interpreted as a measure of the heterogeneity of the micropore size distribution and yields better fits where materials feature a range of differently constituted micropores [51].

$$\Theta = \frac{v_{\mathrm{ads}}(p,T)}{v_{\mathrm{mi}}} = \exp\left[-\left(\frac{R\,T\,\ln\left(\frac{p_0}{p}\right)}{E}\right)^n\right] \tag{3}$$

Eq. (3) relates the filled micropore volume fraction Θ to the adsorption potential according to Polanyi: $A = RT\ln(p_0/p)$. Prior to the application of the DA equation, experimental adsorption loadings q_{ads} must be converted to an adsorbed volume v_{ads} considering the saturated-liquid density of CO_2 at adsorption temperature $\rho_{\mathrm{m,liq,CO_2}}(T = 273.15\,\mathrm{K}) = 21.073\,\mathrm{kmol\,m^{-3}}$ [44] assuming sub-critical micropore filling (Eq. 4).

$$v_{\mathrm{ads}}(p,T) = \frac{q_{\mathrm{ads}}(p,T)}{\rho_{\mathrm{m,liq,CO_2}}} \tag{4}$$

The adsorbed volume $v_{\mathrm{ads}}(p,T)$ can be analyzed using the logarithmic form of Eq. (3) by adjusting the heterogenity constant n, while the micropore volume v_{mi} and the characteristic energy of adsorption E are determined from the slope and y-intercept of the DA equation (Eq. 5).

$$\log\left(\frac{v_{\mathrm{ads}}(p,T)}{\mathrm{cm^3\,g^{-1}}}\right) = \log\left(\frac{v_{\mathrm{mi}}}{\mathrm{cm^3\,g^{-1}}}\right) - \left(\frac{1}{\log(e)}\right)^{n-1} \cdot \left(\frac{R\,T}{E}\right)^n \left[\log\left(\frac{p_0}{p}\right)\right]^n \tag{5}$$

In a previous study, Wedler and Span [32] studied the adsorption of CO_2 on biomass chars and applicability of DA and DR theories with different assumptions in the calculations of the pore surface area. They found that the assumptions of uniform slit pores or monolayer coverage were not suitable for heterogeneous and amorphous pore structures. Consequently, we used the approach proposed by Medek et al. [57] using the expression of the adsorption potential with $A = k_{\mathrm{CO_2}}/r_{\mathrm{e}}^{-3}$, where r_{e} is the equivalent pore radius and $k_{\mathrm{CO_2}}$ the interaction constant. The equivalent pore radius represents the average distance of adsorbate molecules from the pore walls and can be calculated as $2v_{\mathrm{mi}}/S_{\mathrm{DA}}$. Differentiation of Eq. (3) with $d\Theta/dr_{\mathrm{e}}$ and integration with respect to the entire pore range, yields the pore surface area S_{DA} resulting from a pore size distribution in the manner of Euler's gamma function (Eq. 6).

$$S_{\mathrm{DA}} = 2v_{\mathrm{mi}}\left(\frac{E}{k_{\mathrm{CO_2}}}\right)^{1/3}\Gamma\left(\frac{3n+1}{3n}\right) \tag{6}$$

3.3. Density functional theory

Recently, major progress in the field of pore structure analysis was made with density functional theory (DFT) calculations, which account for the inhomogeneous behavior of fluids in confined spaces [15,58]. In DFT calculations, the statistical grand canonical ensemble is considered in terms of a grand potential functional $\Omega[\rho(r)]$, defined by a density profile in the pore volume $\rho(r)$ along the pore width r [59]. The density profile at adsorption equilibrium, where the chemical potential μ, the volume V, and the temperature T are constant, is obtained by minimizing $\Omega[\rho(r)]$. For an inhomogeneous fluid in a confined pore space, the grand potential functional can be expressed with the Helmholtz free energy functional of the fluid $F[\rho(r)]$ and the external potential induced by the wall $V_{\mathrm{ext}}(r)$:

$$\Omega[\rho(r)] = F[\rho(r)] - \int \mathrm{d}r\,\rho(r)\,[\mu - V_{\mathrm{ext}}(r)] \tag{7}$$

Lastoskie et al. [60] and Tarazona et al. [61] improved the description of the density profile by explicitly accounting for short-range density correlations, particularly important near the pore wall where density fluctuations are significant. In non-local DFT (NLDFT) applications, various smoothing functions are employed to capture these short-range dependencies of the density profile. In pore structure analysis, the experimental adsorption isotherm can be seen as a composite of theoretical kernels, built up by fluid densities $\rho(p,w)$ and a function for the pore size distribution $f(w)$ forming the adsorption integral equation [59]. Jagiello [62] proposed a solution algorithm for the adsorption integral equation using spline functions, which is widely used in the field [28,31,33] and has been integrated into the software package SAIEUS by *Micromeritics*. Starting with single adsorption isotherm analysis, Jagiello et al. [63] introduced dual-gas analysis to extend the accessible pore size range, while yielding statistically more robust solutions and retaining the full information of experiments [64]. Major improvements in fitting carbon slit pore models were introduced by consideration of the spatial non-uniformity of surfaces [31,65]. In particular, geometric extensions were introduced in terms of a corrugated surface (2D), which was found suitable for turbostratic porous carbons with corrugated slit pores [28]. Furthermore, energy heterogeneity considering spatial variation of the surface side energy was introduced. In the latest version of SAIEUS (3.2) [62], numerous NLDFT kernels are implemented and were applied recently to heterogeneous biomass chars using different probe gases [64,66]. SAIEUS and the gas-specific 2D-NLDFT kernels reported [31,64,65,67] were used in this study to integrate the spline functions. 2D-NLDFT calculations generally yield multiple valid solutions. Each solution corresponds to a specific value of a regularization parameter λ, adjustable through the GUI of SAIEUS. The resulting solutions can be represented by an L-curve, relating the degree of smoothing of the resulting PSD to the quality of the fit to the experimental data. The L-curve criterion [68] can be used to identify solutions providing a reasonable balance between goodness of fit and the degree of PSD smoothing. However, the criterion does not uniquely determine a single solution and typically yields a range of acceptable λ values. In this study, λ was selected from the range suggested by the L-curve criterion, giving preference to the smoothest PSDs, as these generally provide a more realistic representation of heterogeneous pore structures [69]. A representative L-curve plot incorporating the chosen solution for the O_2 & H_2 2D-NLDFT analysis for MCC-HTC-800 is presented in Figure S3 in *Supplementary Information*.

The detectable pore size range of NLDFT depends on the considered thermodynamic behavior of the probe gas under the respective measurement conditions. The range between the maximum experimental

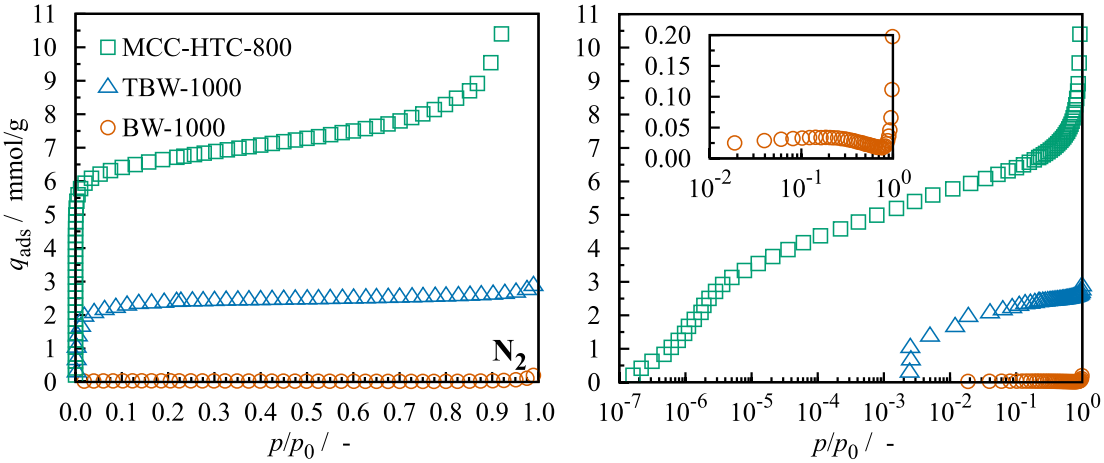


Fig. 2. Experimental N_2 adsorption isotherms at 77 K for MCC-HTC-800, TBW-1000, and BW-1000 shown with (left) a linear and (right) a logarithmic relative pressure axis.

pressure p_{max} and the saturation pressure at adsorption temperature p_0 (Table 2) usually indicates the resolvable pore size range. The upper pore size limit is reached when the theoretical, pore-size-resolved isotherms become similar to each other with increasing pore size and approach the adsorption behavior on flat surfaces showing insensitivity to higher pore width [30]. In micropore analysis, H_2 adsorption up to $p = 100$ kPa is sensitive to a pore width range of 0.8 to 1.5 nm [28,30,33], while CO_2 data measured up to $p/p_0 = 0.03$ cover pores up to 1 nm [15,17]. In principle, if CO_2 adsorption were measured up to $p = 3485.1$ kPa ($p/p_0 = 1$), pores with maximum widths of 10 nm could be resolved, since adsorption weakens for larger pores due to the proximity to the critical point. Pores up to a width of 50 nm can be resolved by N_2 and O_2 adsorption measurements performed close to $p/p_0 = 1$ [67]. As suggested by Jagiello et al. [64,67] and Blankenship et al. [28], the lowest detectable pore size with respect to their kinetic diameter d_k is 0.3 nm for H_2 and 0.36 nm for N_2, O_2, and CO_2. In the practical application of models in SAIEUS, the lowest accessible pore size w_{min} can be restricted as experimental data might be characterized by pore blockage in the low-pressure range.

4. Results and discussion

4.1. Adsorption isotherms

The N_2 adsorption capacity at 77 K of MCC-HTC-800 exceeds the moderate adsorption loading of TBW-1000, whereas BW-1000 shows no detectable adsorption (Fig. 2). The adsorption isotherm of MCC-HTC-800 exhibits a very sharp increase in the low-pressure region, indicating a high fraction of micropores, followed by a consistent increase in the mid-pressure range, corresponding to a Type II isotherm. In contrast, TBW-1000 shows a Type I(b) behavior. For MCC-HTC-800, a gradual increase and a stronger pore condensation tendency are observed near $p/p_0 = 1$, reflecting a broader pore size distribution extending into the mesopore-regime ($2 < w_{pore} < 50$ nm). A notable difference from TBW-1000 is that pore filling occurs at $p/p_0 \approx 2\times10^{-3}$ compared to 2×10^{-7} for MCC-HTC-800 using the same dosing amount (Table S1), indicating that the smallest pores are either not present, not detectable or not accessible. The BW-1000 isotherm shows no detectable adsorption capacity, indicating significantly reduced micro-porosity, blocked pores or drastically slowed diffusion. One possible explanation is that pore space is reduced due to bonding of hemicellulose structures during heat treatment, hindering the free arrangement of aromatic layers [3]. The negative slope (Fig. 2) is an artifact resulting from the free space volume correction in combination with negligible adsorption loading. The persistent problem of slow N_2 diffusion at 77 K in narrow micropores of heterogeneous carbons [22–24] is consistent with the long measurement duration of 68 h for MCC-HTC-800 and TBW-1000.

The CO_2 adsorption isotherms at 273 K for TBW-1000 and MCC-HTC-800 show distinct adsorption tendencies with a maximum adsorption loading of 2.74 and 3.37 mmol/g at $p/p_0 = 0.035$. The MCC-HTC-800 data measured in this work are in excellent agreement with the experimental results reported by Wedler and Span [32], while for TBW-1000, the data show a small deviation at higher pressures. Although Wedler and Span used identical samples, the observed deviations in the results may be attributed to structural changes caused by repeated thermal treatments during the degassing procedure. For BW-1000, a comparatively smaller maximum adsorption loading of $q_{ads} = 1.75$ mmol/g was obtained, which is still significant compared to the negligible adsorption tendency of N_2. In experiments with CO_2 at 273 K, diffusion or pore filling limitations are expected to be significantly lower compared to experiments with N_2 due to the elevated adsorption temperature, higher absolute pressures at the low-pressure end of the isotherm, smaller kinetic diameter (Table 2) and higher adsorption energy. CO_2, however, has a higher quadrupole moment than N_2 and may undergo stronger interactions with surface functional groups. The high oxygen fraction ($w_O = 42.15$ %) in BW-1000 (Table 1) suggests a considerable amount of surface functional groups, which are typically decomposed during pyrolysis but may still be present to a certain extent [70]. This surface constitution can enhance CO_2 adsorption and distort the determination of unbiased porosity in functionalized carbons [71].

The shape of the O_2 adsorption isotherms obtained at 77 K for MCC-HTC-800 and TBW-1000 (Fig. 4) is comparable to N_2, whereas TBW-1000 shows significantly higher adsorption capacity and pore filling at much lower relative pressures $p/p_0 \approx 2\times10^{-6}$. This indicates that TBW-1000 has ultramicropores, which are not accessible to N_2. The duration of the O_2 measurements (Table S1) was comparatively long, especially with TBW-1000, indicating slow diffusion of O_2 molecules at low relative pressures. However, a low dosing amount of $q_d = 0.05$ mmol/g (Table S1) was maintained to resolve the low pressure region of the isotherm at the expense of significantly longer measurement times. BW-1000 shows very low adsorption tendency, which was, however, detectable by enhancing the dosing amount q_d to 0.1 mmol/g (Table S1). The adsorption capacity of MCC-HTC-800 for N_2 and O_2 is in good agreement with results from Korus et al. [29], who analyzed the pore structure of straw pellet chars from gasification experiments. At $p/p_0 \approx 0.5$, they measured for a G1000 char an adsorption loading of $q_{ads} = 6.5 - 6.7$ mmol/g with N_2 and $q_{ads} = 8.0 - 8.3$ mmol/g with O_2 [29].

The H_2 adsorption isotherms at 77 K for MCC-HTC-800 and TBW-1000 show, with $q_{ads} = 6.14$ and 4.87 mmol/g, higher adsorption

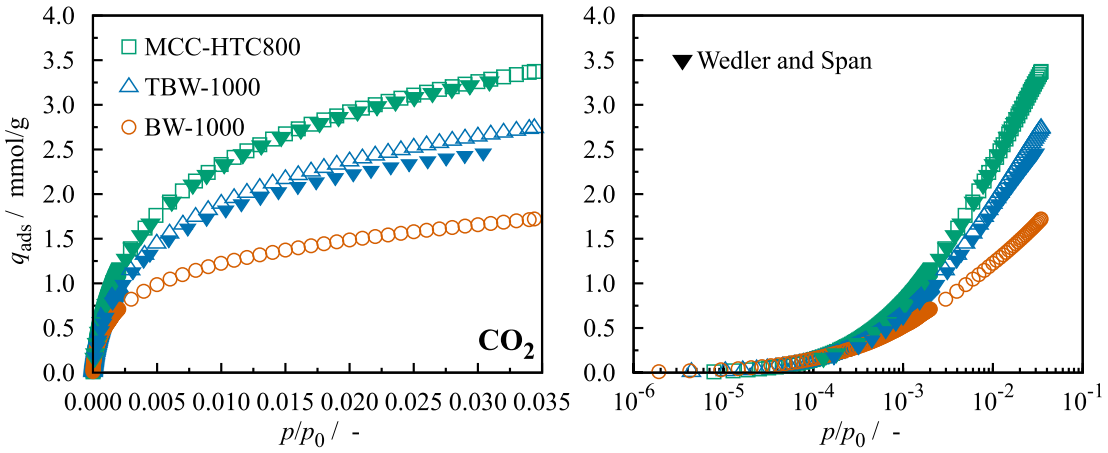


Fig. 3. Experimental CO_2 adsorption isotherms at 273 K for MCC-HTC-800, TBW-1000, and BW-1000 in comparison to data reported by Wedler and Span [32] shown with (left) a linear and (right) a logarithmic relative pressure axis.

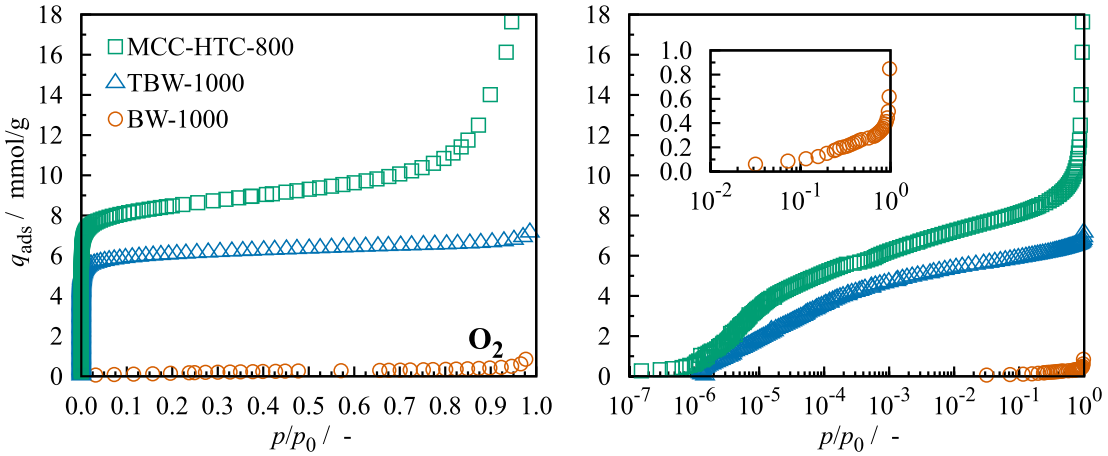


Fig. 4. Experimental O_2 adsorption isotherms at 77 K for MCC-HTC-800, TBW-1000, and BW-1000 shown with (left) a linear and (right) a logarithmic relative pressure axis.

loadings compared to CO_2 at $p = 100$ kPa, whereby H_2 adsorption was measured at a considerably lower temperature. In contrast, BW-1000 shows lower H_2 adsorption affinity compared to CO_2. Taking the very distinct quadrupolar moment of $\mu = -13.71 \times 10^{40}\,\mathrm{cm}^2$ for CO_2 compared to $\mu = 2.2 \times 10^{40}\,\mathrm{cm}^2$ for H_2 into account, the assumption can be reinforced that the potential surface functionality promotes the adsorption of CO_2. The supercritical adsorption temperature and small size of H_2 enhance diffusion, while the adsorption process is limited to surface adsorption, enabling efficient probing without condensation even in the smallest pores [33]. Blankenship et al. [28] conducted H_2 adsorption studies on hydrothermal carbonized sawdust samples reporting adsorption loadings in the same order of magnitude compared with experiments in this study. Different studies on activated carbon materials [30,64] report H_2 and CO_2 adsorption capacities comparable to those of MCC-HTC-800 and TBW-1000.

4.2. BETSI analysis

For the BET analysis, the IUPAC standard [16] suggests a relative pressure range of the isotherm of $p/p_0 = 0.05 - 0.3$ for the formation of a monomolecular adsorption layer. However, for the investigated biomass chars a material-specific range of p/p_0 intervals, varying in both length and position along the adsorption isotherm, was found with BETSI. The identified relative pressure intervals and corresponding fits of Eq. (1) are shown exemplarily for the N_2 data of MCC-HTC-800 and TBW-1000 in Fig. 6. Details on the O_2 analysis can be found in Figure S1 in *Supplementary Information*.

The BETSI surface areas S_{BETSI} based on N_2 and O_2 adsorption data are presented along with all fitted parameters in Table 3. Comparing the results for both adsorptives, O_2 yields a larger surface area, which in the case of TBW-1000 is more than three times as large as with N_2. The values of n_m are governed by the adsorbed amount in the BET relative pressure range and are systematically higher for O_2. This indicates that the ability to probe the smallest pores in experiments directly influences the resulting pore surface area. The BW-1000 char could not be analyzed due to insufficient adsorption of N_2 and O_2. The statistical uncertainty of the BET parameters C and n_m was assessed with a bootstrap resampling procedure, which is discussed in more detail in *Supplementary Information*. The statistical uncertainty of C is very high across all conducted BETSI analyses (see Table 3). This parameter shows a high sensitivity to variations of the regression intercept a with $C = 1 + b/a$, where a is on the order of 10^{-5} for all investigated isotherms. The monolayer capacity n_m, in contrast, exhibits a substantially lower uncertainty as the intercept a contributes only marginally to its calculation via $n_m = 1/(a + b)$ and the statistically more robust slope b dominates the resulting n_m. This behavior reflects the theoretical limit of high C values effectively reducing the BET equation to single-point characteristics, where it is questionable, whether a specific value of n_m during micropore filling reflects a genuine monolayer occupation and provides reliable information on the micropore surface area.

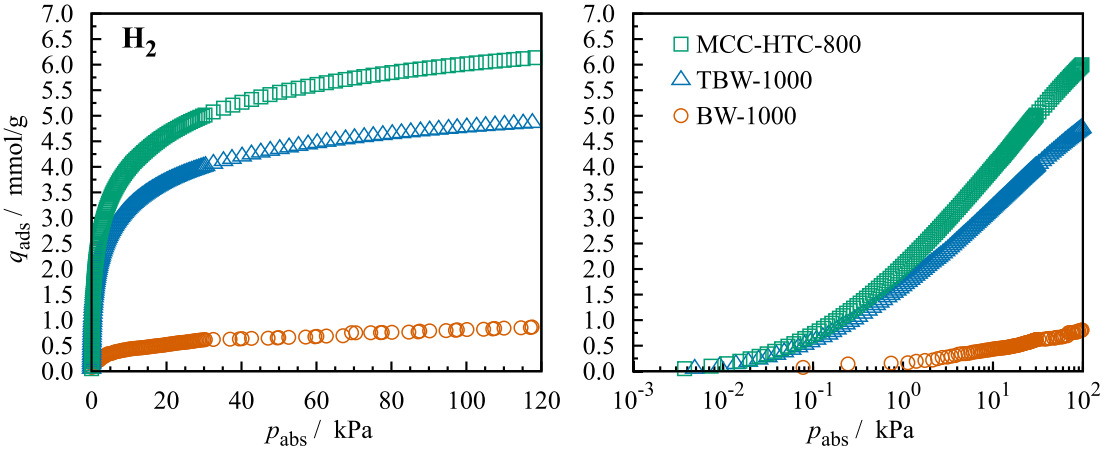


Fig. 5. Experimental H_2 adsorption isotherms at 77 K for MCC-HTC-800, TBW-1000, and BW-1000 shown with (left) a linear and (right) a logarithmic relative pressure axis.

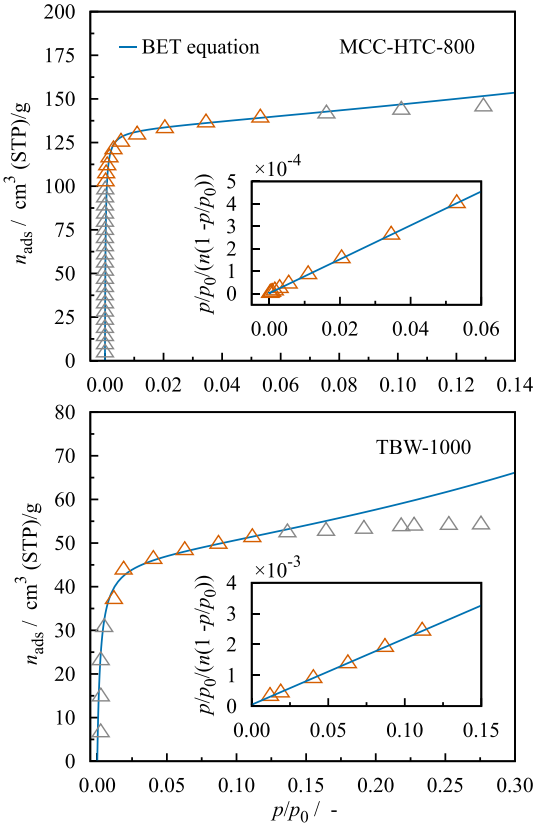


Fig. 6. Experimental adsorption loadings of N_2 at 77 K and the BET fits in the identified BET range by BETSI (Orange triangles). The Corresponding linear forms of the BET fits and the converted experimental data are shown in the insets. (For interpretation of the references to colour in this figure legend, the reader is referred to the web version of this article.)

4.3. DA analysis

The experimental adsorbed volumes in their logarithmic form and the corresponding DA-fits are shown in Fig. 7, whereas the parameters n and E are given in Table 4. All plots show pronounced linearity over the entire experimental range. MCC-HTC-800 exhibits the highest value of the heterogeneity constant (n = 2.27) compared to the other samples, which show values closer to n = 2, suggesting a broader pore size distribution. As the characteristic energies of adsorption E and the equivalent pore radii r_e are very similar across the samples (Table 4), the pore structures appear to be highly comparable. The specific surface area calculated with Medek's equation (Eq. 6) enables an assessment of the pore structure characteristics for BW-1000. The specific surface areas S_{DA}, as reported in Table 4, are larger compared to the BETSI surface areas, suggesting that more pores of smaller size can be probed by CO_2.

4.4. 2D-NLDFT analysis

The 2D-NLDFT single and dual-gas analyses yield pore-size-resolved cumulative pore surface area S_{cum} and volume v_{cum} as well as their differentials dv/dw and dS/dw. The pore size range accessible by 2D-NLDFT is limited by the underlying adsorption measurement and typically covers pores up to w_{pore} = 50 nm [16]. Therefore, a complete characterization of the pore structure generally requires complementary techniques, such as MIP and He pycnometry. Tables 5 and 6 report the cumulative properties for the entire PSD covered by the respective models. Figs. 8 to 14 provide insight into the pore-size-specific contributions, which depend directly on the ability of the 2D-NLDFT models to reproduce the experimental adsorption isotherms.

4.4.1. Single-gas 2D-NLDFT

In this section, the potential of single-gas analysis as an alternative to BETSI and DA is demonstrated using N_2 and CO_2 adsorption isotherms. Fig. 8 compares N_2- and CO_2-2D-NLDFT results for MCC-HTC-800 and TBW-1000. For MCC-HTC-800, N_2 and CO_2 fits yield almost the same cumulative pore volume v_{cum} up to $w_{max,CO2}$ = 1 nm. In the respective pore size range, the N_2 fit yields a unimodal contribution, while the CO_2 analysis shows a bimodal PSD. However, the majority of the pore volume of MCC-HTC-800 corresponds to the pores with w_{pore} > 10 nm, which are only detectable by N_2 measurements. In the evaluation of TBW-1000, a minimum pore width of $w_{min,N2}$ = 0.76 nm was found to be the most suitable to represent the restricted accessibility of pores to N_2. Consequently, the resulting PSD shows no contribution below w_{pore} = 1 nm, while CO_2-2D-NLDFT yields a significantly higher contribution in the ultramicropore regime (Table 5). The analysis of BW-1000 based on the CO_2-isotherm (Fig. 9) reveals a bimodal PSD comparable with MCC-HTC-800 and TBW-1000. However, the cumulative pore volumes differ significantly (Table 5) and show a clear correlation with the CO_2 adsorption loading (Fig. 3).

Comparing the BET surface area S_{BETSI} for MCC-HTC-800 with the cumulative pore surface area S_{cum}, a significant difference of 170 m^2/g can be observed. As the N_2 isotherm shows strong adsorption behavior in the low-pressure range beyond the BET range of 2.0×10^{-4} <

Table 3
Best-fit parameters $C(-)$ and $n_m(cm^3(STP)/g)$ obtained from the BETSI analysis of MCC-HTC-800 and TBW-1000 based on experiments at 77 K with N_2 and O_2. The Corresponding specific surface area $S_{BETSI}(m^2/g)$ is calculated on basis of n_m according to Eq. (2). The standard deviations $\sigma(C)$ and $\sigma(n_m)$ are obtained from statistical analysis using the bootstrap resampling procedure.

Material	Adsorptive	p/p_0	C	$\sigma(C)_{bootstrap}$	n_m	$\sigma(n_m)_{bootstrap}$	S_{BETSI}
MCC-HTC-800	N_2	$2.0\times10^{-4}-5.3\times10^{-2}$	4766.6	995.8	132.2	0.23	575.8
	O_2	$4.5\times10^{-3}-4.9\times10^{-2}$	2051.6	59.4	168.7	0.10	639.3
TBW-1000	N_2	$1.2\times10^{-2}-1.1\times10^{-1}$	451.6	90.0	46.4	0.27	202.2
	O_2	$7.3\times10^{-4}-4.3\times10^{-2}$	4154.2	259.0	123.2	0.12	466.8

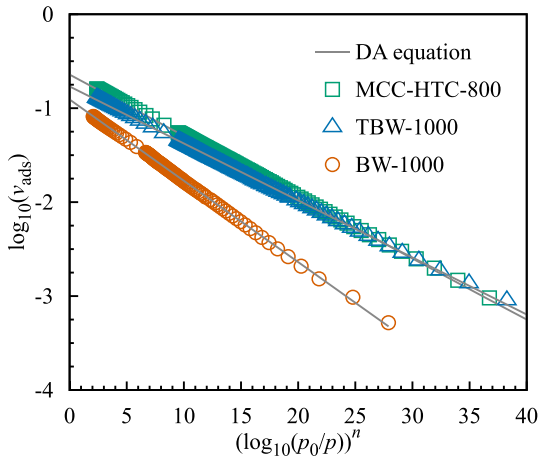


Fig. 7. DA fits and converted experimental data for the adsorption of CO_2 at 273 K for MCC-HTC800, TBW-1000, and BW-1000.

Table 4
Best-fit parameters n and associated DA equation parameters v_{mi} and E, along with the DA specific surface areas S_{DA} and equivalent pore radii r_e for MCC-HTC-800, TBW-1000, and BW-1000.

Material	v_{mi} / cm^3/g	E / kJ/mol	n / –	r_e / nm	S_{DA} / m^2/g
MCC-HTC-800	0.228	12.053	2.27	0.684	666.0
TBW-1000	0.201	11.631	2.09	0.677	577.1
BW-1000	0.124	12.174	1.91	0.688	359.6

$p/p_0 < 5.3\times10^{-2}$ (Table 3), it can be assumed that N_2-2D-NLDFT resolves the high contribution of ultramicropores to the overall surface area and, therefore, yields a higher cumulative surface area S_{cum}. In contrast, N_2-2D-NLDFT for TBW-1000 results in a smaller cumulative pore surface area compared to the BET value. As the low-pressure region is only resolved by experimental data for $p/p_0 > 2\times10^{-3}$ (Fig. 2), the effect described above may be of minor significance. The apparent surface area S_{BETSI} is instead artificially enhanced through the assumption of monolayer coverage of the pore surface involving the same adsorption amount, which in reality rather forms a denser adsorbed phase in heterogeneous micropores.

The CO_2-2D-NLDFT calculations provide a detailed PSD in the ultramicropore regime, allowing the smallest pores to contribute to the pore surface area compared to the simple pore size distribution assumed by Medek [57]. For BW-1000, the cumulative pore surface area and volume obtained from CO_2-2D-NLDFT (Tables 5) and the respective DA results (Tables 4) are rather close to each other. As the micropore loading rises from BW-1000 to TBW-1000 and further to MCC-HTC-800 (Fig. 3), the discrepancies between DA and CO_2-2D-NLDFT values become more pronounced, with S_{DA} remaining lower than S_{cum} and v_{mi} consistently exceeding v_{cum}. As Medek [57] assumes a broad unimodal PSD, small pores are underrepresented and large pores overrepresented compared

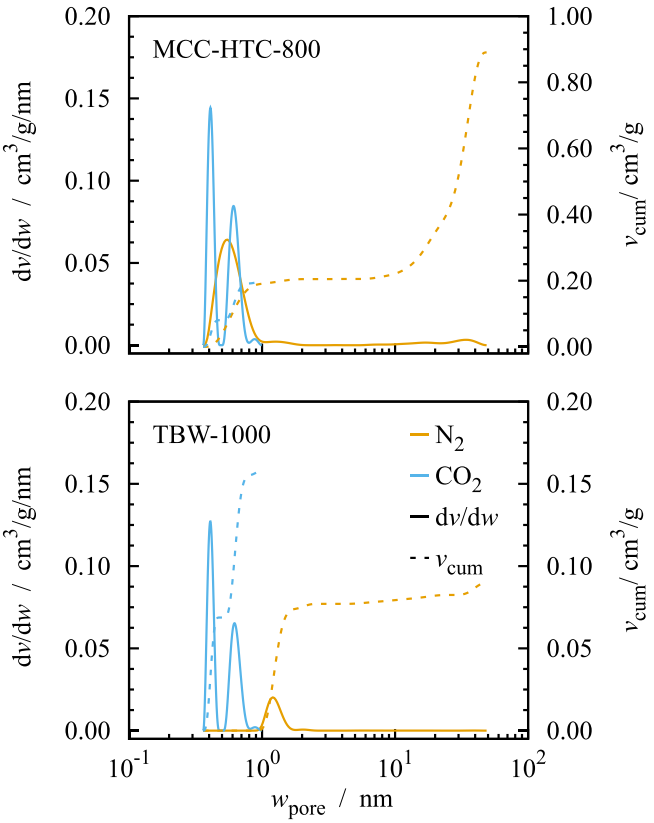


Fig. 8. Results of single-gas 2D-NLDFT analysis for MCC-HTC-800 and TBW-1000.

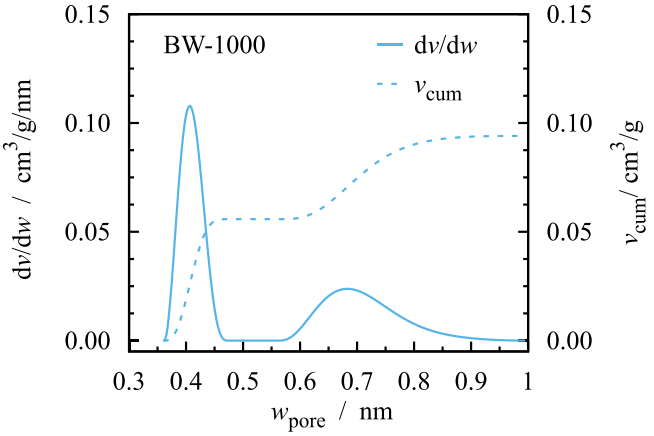


Fig. 9. Results of CO_2-2D-NLDFT analysis for BW-1000.

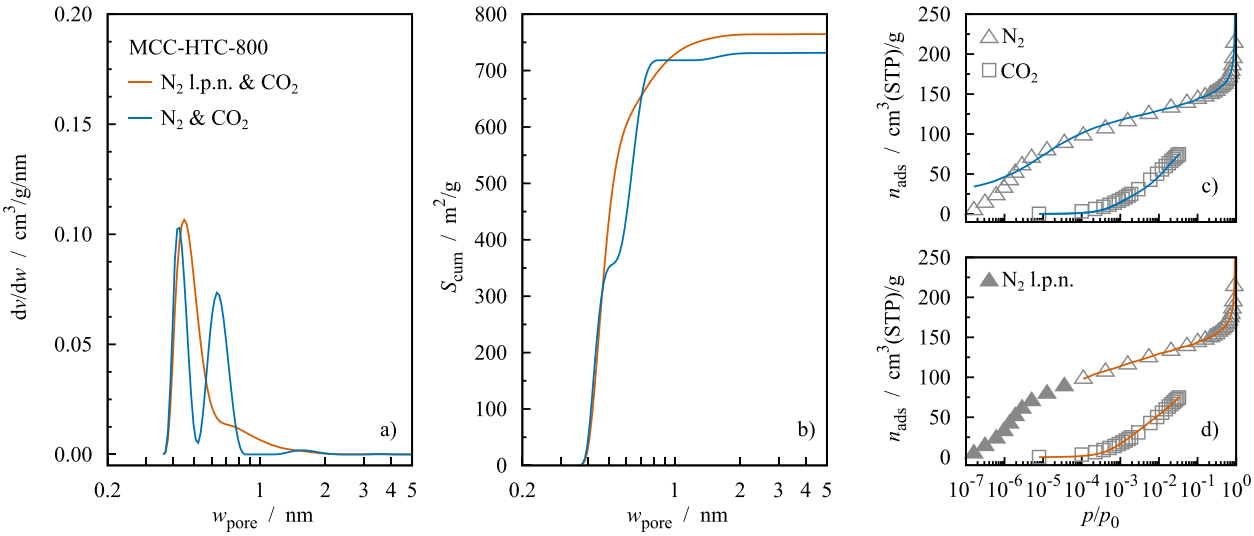


Fig. 10. PSD for MCC-HTC-800 obtained from N_2 & CO_2 dual-gas 2D-NLDFT fits (a) and b)) with consideration of the full N_2 adsorption isotherm (c)) and with neglect of the low-pressure data (d)).

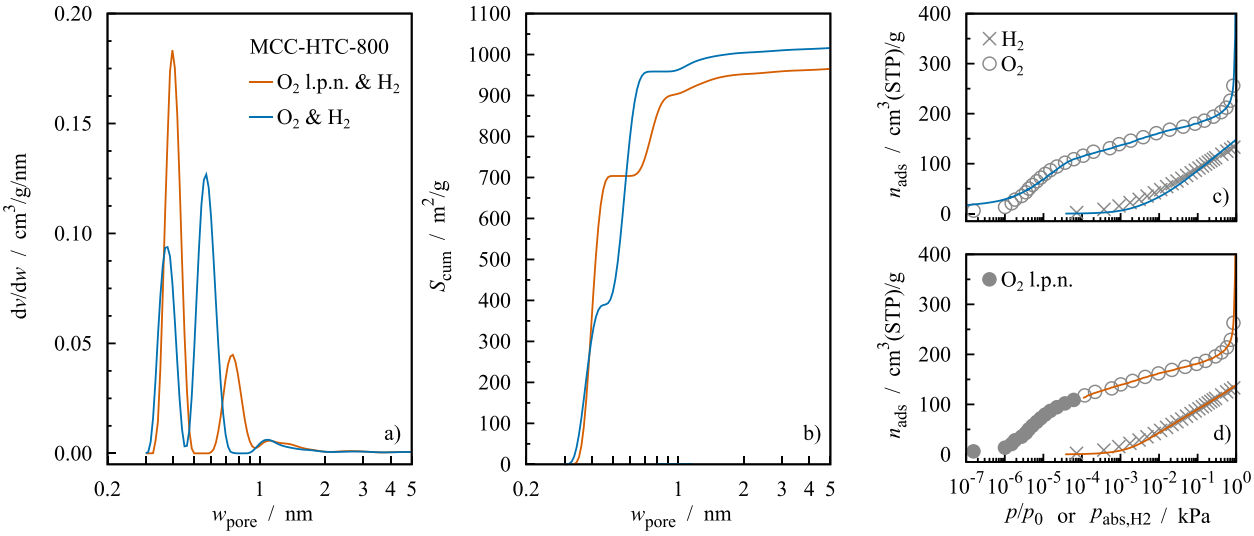


Fig. 11. PSD for MCC-HTC-800 obtained from O_2 & H_2 dual-gas 2D-NLDFT fits (a) and b)) with consideration of the full O_2 adsorption isotherm (c)) and with neglect of the low-pressure data (d)).

to CO_2-2D-NLDFT, resulting in these deviations in pore surface area and volume.

4.4.2. *Dual-gas 2D-NLDFT*

The dual-gas analysis takes advantage of the different pore size sensitivities of two probe gases in a simultaneous fit. Combinations of micropore isotherms (CO_2 or H_2) with N_2 or O_2 are recommended, thus this study focuses on the commonly applied pair of CO_2 & N_2 and the rarely demonstrated pair of H_2 & O_2.

As emphasized in studies by Jagiello et al. [31,64], the 2D-NLDFT kernels are correlated within the pore size range where both probe gases are sensitive, affecting the low-pressure region of the N_2 and O_2 data as well as a major portion of the respective CO_2 and H_2 adsorption isotherms. The consistency of data in the overlapping pore size range of 2D-NLDFT analysis can be assessed by comparing shortened and full N_2 and O_2 isotherms in dual-gas analysis, as demonstrated by Jagiello et al. [31,64]. Inconsistent data significantly deteriorate the simultaneous fit of both kernels, leading to a systematic underestimation of one adsorption isotherm and overestimation of the other. In the analysis of carbons with narrow ultramicropores, the two probe gases may exhibit different sensitivities or accessibility to such pores, resulting in discrepancies [31,64]. To evaluate the impact of this effect on the systems studied, the differences between analyses with and without low-pressure data (l.p.n.) are examined for MCC-HTC-800 as an example. The N_2 and O_2 isotherms are truncated at $p/p_0 < 10^{-4}$, which approximately corresponds to the pore-filling pressure of N_2 in carbonaceous micropores with a width of 1 nm [72]. The omitted low-pressure region is covered by the second isotherm (CO_2 or H_2), which is more sensitive to pores up to approximately 1 nm in width as described in Section 4.4.1. The results are shown in terms of the cumulative pore properties in Table 6 and supported by Fig. 10 for N_2 and CO_2 and Fig. 11 for O_2 and H_2 with a focus on changes in the PSD in the ultra/micropore regime below $w_{pore} = 5$ nm.

The N_2 & CO_2 dual-gas analysis results in an overprediction of N_2 data for $p/p_0 < 2.0 \times 10^{-6}$ as shown in the fit plots in Fig. 10(c). At the same time, the representation of the CO_2 data in the pressure range $10^{-4} < p/p_0 < 10^{-2}$ is slightly deteriorated, indicating a discrepancy between the datasets and the correlated models used in the dual-gas analysis. The N_2 data are likely underestimated in the low-pressure region due to diffusion limitations and therefore do not fully

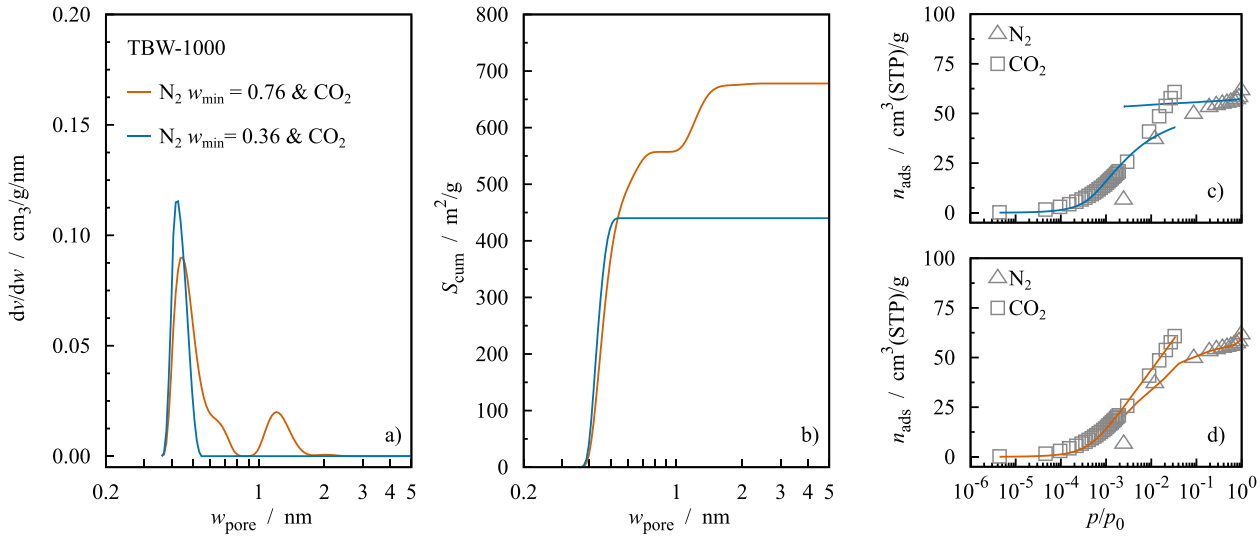


Fig. 12. PSD for TBW-1000 obtained from N_2 & CO_2 dual-gas 2D-NLDFT fits (a) and b)) with two different minimum pore widths $w_{min,N2}$ considered for the N_2 model (c) and d)).

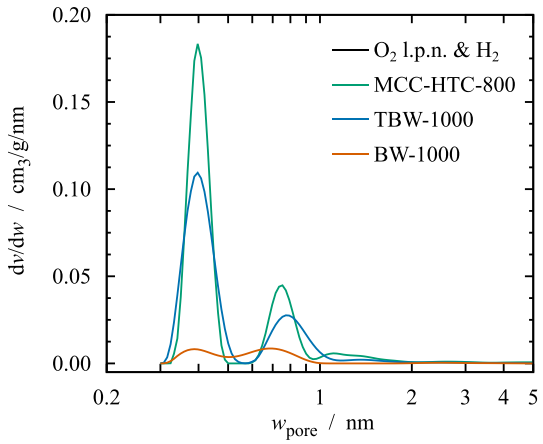


Fig. 13. PSD for MCC-HTC-800, TBW-1000, and BW-1000 obtained from O_2 & H_2 dual-gas 2D-NLDFT fits with neglect of the low-pressure data.

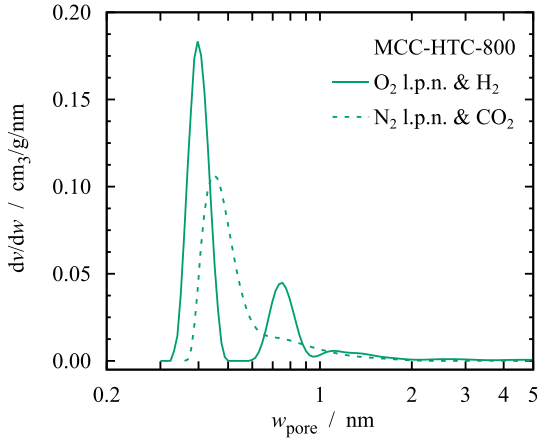


Fig. 14. PSD for MCC-HTC-800 obtained from H_2 & O_2 and N_2 & CO_2 dual-gas 2D-NLDFT fits with neglecting low-pressure data.

Table 5
Cumulative pore surface area S_{cum} and volume v_{cum} from single-gas (N_2 and CO_2) 2D-NLDFT analysis in the pore size range of 0.36 nm< w_{pore} < 50 nm.

Material	Isotherm	2D-NLDFT settings			2D-NLDFT results	
		w_{min} / nm	w_{max} / nm	λ	S_{cum} / m^2g^{-1}	v_{cum} / cm^3g^{-1}
MCC-HTC-800	N_2	0.36	50.0	3.25	748.5	0.892
	CO_2	0.36	1.0	3.25	759.0	0.196
TBW-1000	N_2	0.76	50.0	3.25	123.6	0.090
	CO_2	0.36	1.0	3.25	614.1	0.158
BW-1000	CO_2	0.36	1.0	3.25	382.0	0.094

match the CO_2 adsorption behavior. This behavior was also observed by Jagiello et al. [66] for dual-gas 2D-NLDFT fits of biomass chars, who proposed increasing the lower pore size limit of the N_2 model isotherm $w_{min,N2}$. An increase to $w_{min,N2}$ > 0.36 results in a negative impact on the overall fit quality. In contrast, neglecting the low-pressure N_2 data leads to a slight improvement in the representation of the CO_2 isotherm (Fig. 10(d)) providing more reliable information on the ultramicropore regime. Figs. 10(a) and 10(b) show the consequences for the resulting PSD. The second of the closely spaced peaks in the N_2 & CO_2 analysis can be attributed to the artificially enhanced contribution of the N_2 model. Neglecting the low-pressure data (l.p.n.) results in a broader peak between 0.36 and 0.6 nm and a smoother transition to the contribution of wider pores. This leads to an enhanced overall pore surface area S_{cum} contributed by the ultramicropore regime (Table 6). The cumulative pore volume v_{cum} is mainly defined by contributions from wider pores covered by the N_2 isotherm at $p/p_0 > 10^{-4}$.

The O_2 & H_2 results show similar behavior in terms of an overprediction of the O_2 data in the low pressure region up to $p/p_0 = 10^{-5}$ (Fig. 11(c)). When considering the entire range of O_2 data in the dual-gas analysis, a value of $w_{min,O2}$ = 0.38 nm yields the best representation of the data. However, only by removing the low-pressure O_2 data, a noticeable improvement in the H_2 data representation across the entire relative pressure range of the isotherm could be achieved (Fig. 11(d). The second dominant peak of the O_2 & H_2 fit is significantly weakened through the neglect of the low-pressure data and shifted to higher pore sizes (Fig. 11(a)), suggesting that the overprediction of the O_2 data in the lowest pressure range causes this artificially inflated contribution at a pore width of w_{pore} = 0.5 to 0.6 nm. The comparatively small

Table 6
Cumulative pore surface area S_{cum} and volume v_{cum} from dual-gas 2D-NLDFT analysis with different gas combinations in the respective pore size range of $w_{min} < w_{pore} < 50$ nm, using full experimental adsorption isotherms and low-pressure data neglection (l.p.n.).

Material	Isotherm 1	Isotherm 2	2D-NLDFT settings			2D-NLDFT results	
			w_{min} / nm	$w_{min,N2/O2}$ / nm	λ	S_{cum} / m^2g^{-1}	v_{cum} / cm^3g^{-1}
MCC-HTC-800	N_2	CO_2	0.36	0.36	3.50	786.10	0.8874
	N_2 l.p.n.	CO_2	0.36	0.36	3.25	819.42	0.8981
	O_2	H_2	0.3	0.38	3.75	1054.8	0.6951
	O_2 l.p.n.	H_2	0.3	0.3	3.00	1004.5	0.6947
TBW-1000	N_2	CO_2	0.36	0.36	3.25	440.55	0.1051
	N_2	CO_2	0.36	0.76	3.25	679.46	0.2255
	O_2	H_2	0.3	0.3	3.75	816.81	0.2374
	O_2 l.p.n.	H_2	0.3	0.3	3.75	793.79	0.2291
BW-1000	O_2	H_2	0.3	0.9	3.50	128.95	0.0533

improvement in the H_2 fit results in a significant enhancement of the contribution of the smallest pores in the range of $0.3 < w_{pore} < 0.5$ nm.

In the TBW-1000 dual-gas 2D-NLDFT analysis, a strong discrepancy between the N_2 and CO_2 model characteristics was observed, as shown in Fig. 12(c). As the N_2 data start at $p/p_0 = 2 \times 10^{-3}$, no appropriate truncation of the low-pressure data was possible. However, a significant improvement in the fit of both isotherms could be achieved by setting $w_{min} = 0.76$ nm (Fig. 12(d)). These results indicate that the smallest pores, which are typically filled at very low pressures, are effectively blocked or inaccessible to N_2. In this context, the evaluation parameter w_{min} appears to be a useful tool, especially when the second probe gas (CO_2) has no restrictions in filling micropores. The significant difference in the cumulative pore surface area of 240 m^2g^{-1} (Table 6) for $w_{min,N2} = 0.76$ nm and 0.36 nm can be attributed exclusively to the PSD contributions for $w_{pore} < 2$ nm. In the O_2 & H_2 dual-gas analysis of TBW-1000, as shown in *Supplementary Information* in Figure S2, similar effects and trends could be observed compared to MCC-HTC-800 and are therefore not further discussed in detail.

A comparison of the PSD results from O_2 l.p.n. & H_2 dual-gas analysis for all samples is shown in Fig. 13. All three chars exhibit comparable pore size contributions to the PSD at $w_{pore} = 0.4$ and 0.7 nm. However, BW-1000 shows a significantly lower contribution across the PSD, particularly for the lowest pore size peak, which can be attributed to the low adsorption tendency of H_2. The dual-gas analysis results for BW-1000 show noticeably lower cumulative pore surface area S_{cum} and volume v_{cum} compared to the single-gas analysis with CO_2 (Tables 5 and 6). This can be attributed to the less pronounced adsorption behavior of H_2 compared to CO_2, which determines the difference in the micropore surface area, as well as the negligible contribution of the O_2 model to the overall pore volume.

To emphasize the difference between both dual-gas combinations (N_2 & CO_2 and O_2 & H_2), the 2D-NLDFT results (l.p.n.) are compared for MCC-HTC-800 in Fig. 14. The H_2 adsorption contributes the very pronounced and strong peak at the lowest pore size, while the CO_2 data yield the first peak at 0.4 nm. The incongruent ultramicropore peak can be attributed to the different pore-probing behavior of the gases. In particular, H_2 exhibits a distinct adsorption behavior (Fig. 5) and is able to diffuse into narrower pores compared to CO_2. The resulting values of the cumulative pore volumes in Table 6 for MCC-HTC-800 strongly depend on the maximum relative pressure reached during the measurements, with N_2 measured up to $p/p_0 = 0.985$ closer to saturation and O_2 up to $p/p_0 = 0.96$. This explains the higher cumulative pore volumes in the N_2 & CO_2 evaluations.

5. Conclusions

In this study, the pore structure of biomass chars was analyzed using different theoretical models that exploit the adsorption properties of probe gases. We emphasized that even by applying an unambiguous BET evaluation strategy, the results are highly dependent on the accessibility of pores for N_2. It further provides a distorted picture of the pore surface area, arising from an inadequate representation of the adsorbed phase behavior in very narrow and heterogeneous ultramicropores. We demonstrated the advantages of using varying probe gases with different sensitivities to the pore structure dominated by ultramicropores. We found that O_2 exhibits a noticeably stronger adsorption affinity than N_2 for all investigated chars. This is reflected in higher loadings for MCC-HTC-800 and TBW-1000, access to smaller pores at very low relative pressures for TBW-1000, and measurable uptake for BW-1000 where N_2 adsorption was negligible. These observations indicate that O_2 shows advantageous diffusion behavior and is therefore better suited for adsorption analysis at cryogenic temperatures over a broad pore size spectrum. Although CO_2 adsorption is well suited for micropore analysis, the resulting evaluation may not solely reflect the pore structure, as it can also be influenced by surface polarities. In contrast, H_2 adsorption is likely to exhibit an intrinsic sensitivity to the pore surface in the narrowest pore regime and is therefore less affected by surface functionalities.

Despite the rather simplified representation of the adsorbed phase density and its distribution in micropores, the applied DA method in combination with Medek's theory provides a straightforward approach for determining pore surface area and volume. Good agreement with results from single-gas 2D-NLDFT analysis can be achieved in cases of comparatively low adsorption capacity, such as for BW-1000. The reliability of single-gas results strongly depends on the adsorption isotherm, as each probe gas defines the accessible pore regimes.

Significant improvement in porosity analysis can be achieved using single-gas 2D-NLDFT evaluations, which require minimal additional effort using CO_2 adsorption isotherms. However, if available, we recommend the application of O_2 or H_2 isotherms for the analysis of biomass chars. The dual-gas 2D-NLDFT analysis expands the analyzable pore size range and is preferable when both isotherms are available and exhibit an equivalent pore surface sensitivity. By paying attention to the data used from the N_2 and O_2 isotherms in the low-pressure region, discrepancies between the two correlated 2D-NLDFT models can be avoided, leading to more reliable PSD results. If available, the pair of O_2 & H_2 can provide the most reliable PSD for biomass chars as H_2 shows fast diffusion in narrow ultramicropores and O_2 brings enhanced pore accessibility.

In conclusion, this study demonstrates that sophisticated pore analyses can provide valuable insights into the pore structure of biomass chars when an appropriate methodological pathway is applied. The comprehensive and reliable pore properties can help to improve the understanding of pore-related reaction rates and morphological changes during conversion. In particular, PSD analyses across different stages of biomass char conversion could enable the validation of pore evolution during conversion, which is particularly relevant for models,

where reaction efficiencies are often correlated to the accessible pore surface area. As different pore regimes may contribute differently to char conversion, resolving their individual contributions can provide valuable input for improving the predictive capability and mechanistic representation of such models [73].

CRediT authorship contribution statement

Tim Eisenbach: Writing – review & editing, Writing – original draft, Visualization, Methodology, Investigation, Formal analysis, Data curation, Conceptualization. **Ehsan Sadeghi Pouya:** Writing – review & editing, Investigation, Formal analysis, Data curation. **Carsten Wedler:** Writing – review & editing, Methodology, Conceptualization. **Erik Freisewinkel:** Writing – review & editing, Investigation, Formal analysis. **Viktor Scherer:** Supervision. **Eric F. May:** Supervision. **Roland Span:** Writing – review & editing, Supervision.

Associated content

The adsorption data are available in a spreadsheet in the Supporting Information.

Declaration of Generative AI and AI-assisted technologies in the writing process

During manuscript preparation, AI tools like ChatGPT and DeepL aided in writing and editing. They helped refine language, enhance clarity and conciseness, standardize terminology, and organize sections based on author-provided content. The AI tools used did not create original scientific ideas, data, or conclusions. All scientific content and decisions were made, verified, and approved by the authors. The authors are fully responsible for the manuscript's accuracy and integrity.

Declaration of competing interest

The authors declare that they have no known competing financial interests or personal relationships that could have appeared to influence the work reported in this paper.

Acknowledgements

This work was funded by the Deutsche Forschungsgemeinschaft (DFG, German Research Foundation) – Project-ID 215035359 – TRR 129 Oxyflame. Gefördert durch die Deutsche Forschungsgemeinschaft (DFG) – Projektnummer 215035359 – TRR 129.

Appendix A. Supplementary data

Supplementary data for this article can be found online at doi:10.1016/j.fuel.2026.140922.

Data availability

Data will be made available upon request.

References

[1] Gil MV, Riaza J, Álvarez L, Pevida C, Rubiera F. Biomass devolatilization at high temperature under N_2 and CO_2: char morphology and reactivity. Energy 2015;91:655–62. https://doi.org/10.1016/j.energy.2015.08.074
[2] Guizani C, Jeguirim M, Gadiou R, Escudero Sanz FJ, Salvador S. Biomass char gasification by H_2O, CO_2 and their mixture: evolution of chemical, textural and structural properties of the chars. Energy 2016;112:133–45. https://doi.org/10.1016/j.energy.2016.06.065
[3] Freisewinkel E, Cerciello F, Eisenbach T, Tarlinski D, Fabozzi A, Schiemann M, Span R, Scherer V, Senneca O. Role of holocellulose on thermal annealing, loss of combustion reactivity and morphological changes in biomass pyrolysis. Fuel 2026;414:138366. https://doi.org/10.1016/j.fuel.2026.138366
[4] Tong W, Liu Q, Yang C, Cai Z, Wu H, Ren S. Effect of pore structure on CO_2 gasification reactivity of biomass chars under high-temperature pyrolysis. J Energy Inst 2020;93:962–76. https://doi.org/10.1016/j.joei.2019.08.007
[5] Avila C, Pang CH, Wu T, Lester E. Morphology and reactivity characteristics of char biomass particles. Bioresour Technol 2011;102:5237–43. https://doi.org/10.1016/j.biortech.2011.01.071
[6] Liu S, Niu Y, Wen L, Kang Y, Wang D, Hui S. Effects of physical structure of high heating-rate chars on combustion characteristics. Fuel 2020;266:117059. https://doi.org/10.1016/j.fuel.2020.117059
[7] Wu R, Beutler J, Price C, Baxter LL. Biomass char particle surface area and porosity dynamics during gasification. Fuel 2020;264:116833. https://doi.org/10.1016/j.fuel.2019.116833
[8] Phounglamcheik A, Bäckebo M, Robinson R, Umeki K. The significance of intraparticle and interparticle diffusion during CO_2 gasification of biomass char in a packed bed. Fuel 2022;310:122302. https://doi.org/10.1016/j.fuel.2021.122302
[9] Wedler C, Span R. A pore-structure dependent kinetic adsorption model for consideration in char conversion – adsorption kinetics of CO_2 on biomass chars. Chem Eng Sci 2021;231:116281. https://doi.org/10.1016/j.ces.2020.116281
[10] Wedler C, Lotz K, Arami-Niya A, Xiao G, Span R, Muhler M, May EF, Richter M. Influence of mineral composition of chars derived by hydrothermal carbonization on sorption behavior of CO_2, CH_4, and O_2. ACS Omega 2020;5:10704–14. https://doi.org/10.1021/acsomega.9b04370
[11] Tarlinski D, Freisewinkel E, Eisenbach T, Span R, Schiemann M, Scherer V. Combustion of single Walnut shell particles in a laminar flow reactor under oxy-fuel conditions: optical measurements and particle sampling. Fuel 2024;369:131613. https://doi.org/10.1016/j.fuel.2024.131613
[12] Holland T, Fletcher TH. Comprehensive model of single particle pulverized coal combustion extended to oxy-coal conditions. Energy Fuels 2017;31:2722–39. https://doi.org/10.1021/acs.energyfuels.6b03387
[13] Freisewinkel E, Eisenbach T, Weise V, Tarlinski D, Pörtner L, Cerciello F, Wedler C, Schiemann M, Span R, Senneca O, Scherer V. Porosity measurement of biomass char by a novel combination of adsorption measurements and an optical method. Int. J. Energy Clean Environ. 2025;27:87–113. https://doi.org/10.1615/InterJEnerCleanEnv.2025056727
[14] Brewer CE, Chuang VJ, Masiello CA, Gonnermann H, Gao X, Dugan B, Driver LE, Panzacchi P, Zygourakis K, Davies CA. New approaches to measuring biochar density and porosity. Biomass and Bioenergy 2014;66:176–85. https://doi.org/10.1016/j.biombioe.2014.03.059
[15] Thommes M, Cychosz KA. Physical adsorption characterization of nanoporous materials: progress and challenges. Adsorption 2014;20:233–50. https://doi.org/10.1007/s10450-014-9606-z
[16] Thommes M, Kaneko K, Neimark AV, Olivier JP, Rodriguez-Reinoso F, Rouquerol J, Sing KS. Physisorption of gases, with special reference to the evaluation of surface area and pore size distribution (IUPAC technical report). Pure Appl Chem 2015;87:1051–69. https://doi.org/10.1515/pac-2014-1117
[17] Dantas S, Struckhoff KC, Thommes M, Neimark AV. Phase behavior and capillary condensation hysteresis of carbon dioxide in mesopores. Langmuir 2019;35:11291–8. https://doi.org/10.1021/acs.langmuir.9b01748
[18] Brunauer S, Emmett PH, Teller E. Adsorption of gases in multimolecular layers. J Am Chem Soc 1938;60:309–19. https://doi.org/10.1021/ja01269a023
[19] Bouchelta C, Medjram MS, Zoubida M, Chekkat FA, Ramdane N, Bellat JP. Effects of pyrolysis conditions on the porous structure development of date pits activated carbon. J Anal Appl Pyrolysis 2012;94:215–22. https://doi.org/10.1016/j.jaap.2011.12.014
[20] Ma Z, Yang Y, Ma Q, Zhou H, Luo X, Liu X, Wang S. Evolution of the chemical composition, functional group, pore structure and crystallographic structure of biochar from palm kernel shell pyrolysis under different temperatures. J Anal Appl Pyrolysis 2017;127:350–9. https://doi.org/10.1016/j.jaap.2017.07.015
[21] Xu D, Cao J, Li Y, Howard A, Yu K. Effect of pyrolysis temperature on characteristics of biochars derived from different feedstocks: a case study on ammonium adsorption capacity. Waste Manag 2019;87:652–60. https://doi.org/10.1016/j.wasman.2019.02.049
[22] Cazorla-Amorós D, Alcañiz-Monge J, Linares-Solano J. Characterization of activated carbon fibers by CO_2 adsorption. Langmuir 1996;12. https://doi.org/10.1021/la960022s
[23] García-Martínez J, Cazorla-Amorós D, Linares-Solano J. Further evidences of the usefulness of CO_2 adsorption to characterize microporous solids. Stud. Surf. Sci. Catal. 2000;128:485–94. https://doi.org/10.1016/S0167-2991(00)80054-3
[24] Garrido J, Linares-Solano J, Martin-Martinez JM, Molina-Sabio M, Rodriguez-Reinoso F, Torregrosa R. Use of nitrogen vs. carbon dioxide in the characterization of activated carbons. Langmuir 1987;3:76–81. https://doi.org/10.1021/la00073a013
[25] Senneca O, Salatino P, Masi S. Microstructural changes and loss of gasification reactivity of chars upon heat treatment. Fuel 1998;77:1483–93. https://doi.org/10.1016/S0016-2361(98)00056-8
[26] Nsakala NY, Essenhigh RH, Walker PL. Characteristics of chars produced from lignites by pyrolysis at 808°C following rapid heating. Fuel 1978;57:605–11. https://doi.org/10.1016/0016-2361(78)90189-8
[27] Gale T, Fletcher TH, Bartholomew CH. Effects of pyrolysis conditions on internal surface areas and densities of coal chars prepared at high heating rates in reactive and non-reactive atmospheres. Energy Fuels 1995;9:513–24. https://doi.org/10.1021/ef00051a017
[28] Blankenship LS, Jagiello J, Mokaya R. Confirmation of pore formation mechanisms in biochars and activated carbons by dual isotherm analysis. Mater Adv 2022;3:3961–71. https://doi.org/10.1039/D2MA00141A
[29] Korus A, Jagiello J, Jensen CD, Sárossy Z, Ravenni G, Benedini L. Advantages of dual CO_2 & O_2 adsorption model for assessment of micropore development in biochar during two-stage gasification. Renew Energy 2024;225:120293. https://doi.org/10.1016/j.renene.2024.120293
[30] Jagiello J, Thommes M. Comparison of DFT characterization methods based on N_2, AR, CO_2, and H_2 adsorption applied to carbons with various pore size distributions. Carbon 2004;42:1227–32. https://doi.org/10.1016/j.carbon.2004.01.022

[31] Jagiello J, Ania C, Parra JB, Cook C. Dual gas analysis of microporous carbons using 2D-NLDFT heterogeneous surface model and combined adsorption data of N_2 and CO_2. Carbon 2015;91:330–7. https://doi.org/10.1016/j.carbon.2015.05.004

[32] Wedler C, Span R. Micropore analysis of biomass chars by CO_2 adsorption: comparison of different analysis methods. Energy Fuels 2021;35:8799–806. https://doi.org/10.1021/acs.energyfuels.1c00280

[33] Beda A, Vaulot C, Matei Ghimbeu C. Hard carbon porosity revealed by the adsorption of multiple gas probe molecules (N_2, AR, CO_2, O_2 and H_2). J Mater Chem A 2021;9:937–43. https://doi.org/10.1039/D0TA10088A

[34] Lotz K, Wütscher A, Düdder H, Berger CM, Russo C, Mukherjee K, Schwaab G, Havenith M, Muhler M. Tuning the properties of iron-doped porous graphitic carbon synthesized by hydrothermal carbonization of cellulose and subsequent pyrolysis. ACS Omega 2019;4:4448–60. https://doi.org/10.1021/acsomega.8b03369

[35] Düdder H, Wütscher A, Stoll R, Muhler M. Synthesis and characterization of lignite-like fuels obtained by hydrothermal carbonization of cellulose. Fuel 2016;171:54–8. https://doi.org/10.1016/j.fuel.2015.12.031

[36] Pielsticker S, Möller G, Gövert B, Kreitzberg T, Hatzfeld O, Yönder, Angenent V, Hättig C, Schmid R, Kneer R. Influence of biomass torrefaction parameters on fast pyrolysis products under flame-equivalent conditions. Biomass and Bioenergy 2018;119:392–410. https://doi.org/10.1016/j.biombioe.2018.08.014

[37] Kreitzberg T, Wirch N, Bormann C, Pielsticker S, Hatzfeld O, Mayer J, Kneer R. Thermally induced changes in microstructure and reactivity of biogenic and fossil fuel particles. Appl Energy 2019;254:113607. https://doi.org/10.1016/j.apenergy.2019.113607

[38] Wang S, Guo X, Wang K, Luo Z. Influence of the interaction of components on the pyrolysis behavior of biomass. J Anal Appl Pyrolysis 2011;91:183–9. https://doi.org/10.1016/j.jaap.2011.02.006

[39] Zhang S, Chen T, Xiong Y, Dong Q. Effects of wet torrefaction on the physicochemical properties and pyrolysis product properties of rice husk. Energy Convers Manag 2017;141:403–9. https://doi.org/10.1016/j.enconman.2016.10.002

[40] Breck DW. Zeolite molecular sieves: structure, chemistry, and use. New York: John Wiley & Sons; 1974.

[41] Rallapalli P, Prasanth KP, Patil D, Somani RS, Jasra RV, Bajaj HC. Sorption studies of CO_2, CH_4, N_2, CO, O_2 and AR on nanoporous aluminum terephthalate [MIL-53(al)]. J Porous Mater 2011;18:205–10. https://doi.org/10.1007/s10934-010-9371-7

[42] Huber ML, Lemmon EW, Bell IH, McLinden MO. The NIST REFPROP database for highly accurate properties of industrially important fluids. Ind. Eng. Chem. Res 2022;61:15449–72. https://doi.org/10.1021/acs.iecr.2c01427

[43] Span R, Lemmon EW, Jacobsen RT, Wagner W, Yokozeki A. A reference equation of state for the thermodynamic properties of nitrogen for temperatures from 63.151 to 1000 K and pressures to 2200 MPa. J Phys Chem Ref Data 2000;29. https://doi.org/10.1063/1.1349047

[44] Span R, Wagner W. A new equation of state for carbon dioxide covering the fluid region from the triple–point temperature to 1100 K at pressures up to 800 MPa. J Phys Chem Ref Data 1996;25. https://doi.org/10.1063/1.555991

[45] Leachman JW, Jacobsen RT, Penoncello SG, Lemmon EW. Fundamental equations of state for parahydrogen, normal hydrogen, and orthohydrogen. J Phys Chem Ref Data 2009;38:721–48. https://doi.org/10.1063/1.3160306

[46] Stewart RB, Jacobsen RT, Wagner W. Thermodynamic properties of oxygen from the triple point to 300 K with pressures to 80 MPa. J Phys Chem Ref Data 1991;20:917–1021. https://doi.org/10.1063/1.555897

[47] Osterrieth JWM, Rampersad J, Madden D, Rampal N, Skoric L, Connolly B, Allendorf MD, Stavila V, Snider JL, Ameloot R, Marreiros J, Ania C, Azevedo D, Vilarrasa-Garcia E, Santos BF, Bu XH, Chang Z, Bunzen H, Champness NR, Griffin SL, Chen B, Lin RB, Coasne B, Cohen S, Moreton JC, Colón YJ, Chen L, Clowes R, Coudert FX, Cui Y, Hou B, D'Alessandro DM, Doheny PW, Dincă M, Sun C, Doonan C, Huxley MT, Evans JD, Falcaro P, Ricco R, Farha O, Idrees KB, Islamoglu T, Feng P, Yang H, Forgan RS, Bara D, Furukawa S, Sanchez E, Gascon J, Telalović S, Ghosh SK, Mukherjee S, Hill MR, Sadiq MM, Horcajada P, Salcedo-Abraira P, Kaneko K, Kukobat R, Kenvin J, Keskin S, Kitagawa S, Otake KI, Lively RP, DeWitt SJA, Llewellyn P, Lotsch BV, Emmerling ST, Pütz AM, Martí-Gastaldo C, Padial NM, García-Martínez J, Linares N, Maspoch D, Del Suárez Pino JA, Moghadam P, Oktavian R, Morris RE, Wheatley PS, Navarro J, Petit C, Danaci D, Rosseinsky MJ, Katsoulidis AP, Schröder M, Han X, Yang S, Serre C, Mouchaham G, Sholl DS, Thyagarajan R, Siderius D, Snurr RQ, Goncalves RB, Telfer S, Lee SJ, Ting VP, Rowlandson JL, Uemura T, Iiyuka T, van der Veen MA, Rega D, van Speybroeck V, Rogge SMJ, Lamaire A, Walton KS, Bingel LW, Wuttke S, Andreo J, Yaghi O, Zhang B, Yavuz CT, Nguyen TS, Zamora F, Montoro C, Zhou H, Kirchon A, Fairen-Jimenez D. How reproducible are surface areas calculated from the BET equation? Adv Mater 2022;34:2201502. https://doi.org/10.1002/adma.202201502

[48] Yang H, Fletcher TH, Li Y, Jin L, Li S, Shang Y, Hu H. Modeling the influence of changes in aliphatic structure on char surface area during coal pyrolysis. Aiche J 2020;66. https://doi.org/10.1002/aic.16834

[49] Schlumberger C, Thommes M. Characterization of hierarchically ordered porous materials by physisorption and mercury porosimetry—a tutorial review. Adv Mater Interfaces 2021;8. https://doi.org/10.1002/admi.202002181

[50] Langmuir I. The adsorption of gases on plane surfaces of glass, mica and platinum. J Am Chem Soc 1918;40:1361–403. https://doi.org/10.1021/ja02242a004

[51] Rouquerol F, Rouquerol J, Sing KS. Adsorption by powders & porous solids. San Diego: Academic Press; 1999. https://doi.org/10.1016/B978-0-12-598920-6.X5000-3

[52] Rouquerol J, Llewellyn P, Rouquerol F. Is the BET equation applicable to microporous adsorbents? Stud. Surf. Sci. Catal. 2007;160:49–56. https://doi.org/10.1016/S0167-2991(07)80008-5

[53] Li S, Yang H, Fletcher TH, Dong M. Model for the evolution of pore structure in a lignite particle during pyrolysis. Energy Fuels 2015;29:5322–33. https://doi.org/10.1021/acs.energyfuels.5b00726

[54] Polanyi M. Über die adsorption vom standpunkt des dritten wärmesatzes. Verh. Dtsch. Phys. Ges. 1914;16:1012–6.

[55] Dubinin MM, Radushkevich LV. The equation of the characteristic curve of activated charcoal. Proc. USSR Acad. Sci. 1947;55:331–5.

[56] Dubinin MM, Astakhov VA. Development of the concepts of volume filling of micropores in the adsorption of gases and vapors by microporous adsorbents. Russ Chem Bull 1971;20:3–7. https://doi.org/10.1007/BF00849307

[57] Medek J. Possibility of micropore analysis of coal and coke from the carbon dioxide isotherm. Fuel 1977;56. https://doi.org/10.1016/0016-2361(77)90131-4

[58] Landers J, Gor GY, Neimark AV. Density functional theory methods for characterization of porous materials. Colloids Surf A Physicochem Eng Asp 2013;437:3–32. https://doi.org/10.1016/j.colsurfa.2013.01.007

[59] Seaton NA, Walton JPRB, Quirke N. A new analysis method for the determination of the pore size distribution of porous carbons from nitrogen adsorption measurements. Carbon 1989;27. https://doi.org/10.1016/0008-6223(89)90035-3

[60] Lastoskie C, Gubbins KE, Quirke N. Pore size distribution analysis of microporous carbons: a density functional theory approach. J Phys Chem 1993;97:4786–96. https://doi.org/10.1021/j100120a035

[61] Tarazona P, Marconi UMB, Evans R. Phase equilibria of fluid interfaces and confined fluids. Mol Phys 1987;60:573–95. https://doi.org/10.1080/00268978700100381

[62] Jagiello J. Stable numerical solution of the adsorption integral equation using splines. Langmuir 1994;10:2778–85. https://doi.org/10.1021/la00020a045

[63] Jagiello J, Ania CO, Parra JB, Jagiello L, Pis JJ. Using DFT analysis of adsorption data of multiple gases including H_2 for the comprehensive characterization of microporous carbons. Carbon 2007;45:1066–71. https://doi.org/10.1016/j.carbon.2006.12.011

[64] Jagiello J, Kenvin J, Ania CO, Parra JB, Celzard A, Fierro V. Exploiting the adsorption of simple gases O_2 and H_2 with minimal quadrupole moments for the dual gas characterization of nanoporous carbons using 2D-NLDFT models. Carbon 2020;160:164–75. https://doi.org/10.1016/j.carbon.2020.01.013

[65] Jagiello J, Olivier JP. 2D-NLDFT adsorption models for carbon slit-shaped pores with surface energetical heterogeneity and geometrical corrugation. Carbon 2013;55:70–80. https://doi.org/10.1016/j.carbon.2012.12.011

[66] Jagiello J, Kenvin J, Celzard A, Fierro V. Enhanced resolution of ultra micropore size determination of biochars and activated carbons by dual gas analysis using N_2 and CO_2 with 2D-NLDFT adsorption models. Carbon 2019;144:206–15. https://doi.org/10.1016/j.carbon.2018.12.028

[67] Jagiello J, Kenvin J. Consistency of carbon nanopore characteristics derived from adsorption of simple gases and 2D-NLDFT models. Advantages of using adsorption isotherms of oxygen (O_2) at 77 K. J Colloid Interface Sci 2019;542:151–8. https://doi.org/10.1016/j.jcis.2019.01.116

[68] Hansen PC, O'Leary DP. The use of the L-Curve in the regularization of discrete ill-posed problems. SIAM J Sci Comput 1993;14:1487–503. https://doi.org/10.1137/0914086

[69] Kupgan G, Liyana-Arachchi TP, Colina CM. NLDFT pore size distribution in amorphous microporous materials. Langmuir 2017;33:11138—-11145. https://doi.org/10.1021/acs.langmuir.7b01961

[70] Saha N, Xin D, Chiu PC, Reza MT. Effect of pyrolysis temperature on acidic oxygen-containing functional groups and electron storage capacities of pyrolyzed hydrochars. ACS Sustain Chem Eng 2019;7:8387–96. https://doi.org/10.1021/acssuschemeng.9b00024

[71] Seredych M, Jagiello J, Bandosz TJ. Complexity of CO_2 adsorption on nanoporous sulfur-doped carbons – is surface chemistry an important factor? Carbon 2014;74:207–17. https://doi.org/10.1016/j.carbon.2014.03.024

[72] Neimark AV, Lin Y, Ravikovitch PI, Thommes M. Quenched solid density functional theory and pore size analysis of micro-mesoporous carbons. Carbon 2009;47:1617–28. https://doi.org/10.1016/j.carbon.2009.01.050

[73] Fatehi H, Bai XS. Structural evolution of biomass char and its effect on the gasification rate. Appl Energy 2017;185:998–1006. https://doi.org/10.1016/j.apenergy.2015.12.093